

pubs.acs.org/cm Article

Orthogonal Nanoprobes Enabling Two-Color Optical Super-Resolution Microscopy Imaging of the Two Domains of Diblock Copolymer Thin Film Nanocomposites

Dana V. Chapman, Joshua A. Hinckley, Jacob A. Erstling, Lara A. Estroff, and Ulrich B. Wiesner*



Cite This: https://doi.org/10.1021/acs.chemmater.1c01204



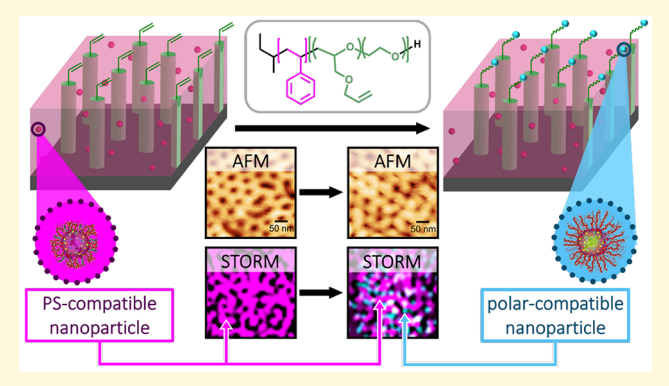
ACCESS

III Metrics & More

Article Recommendations

Supporting Information

ABSTRACT: Multicolor optical super-resolution microscopy (OSRM) describes an emerging set of techniques for the specific labeling of distinct constituents of multicomponent systems with compatible optical probes, elucidating proximity relationships from far-field imaging of diffraction-limited features with nanometer-scale resolution. While such approaches are well established in the study of biological systems, their implementation in materials science has been considerably slower. In large part, this gradual adoption is due to the lack of appropriate OSRM probes that, e.g., by facile mixing or surface modification, enable orthogonal labeling of specific nanostructures in the condensed state, rather than in aqueous conditions as with biology. Here, OSRM probes in the form of ultrasmall (diameters <10 nm) aluminosilicate nanoparticles



encapsulating different fluorescent dyes are tailored to visualize both nanodomains of polystyrene-block-poly[(allyl glycidyl ether)-co-(ethylene oxide)] (PS-b-P(AGE-co-EO)) diblock copolymer thin films. Careful design of nanoprobe surface chemical properties facilitates either selective compatibilization with the nonpolar PS matrix or preferential reactivity with surface allyl groups of the hydrophilic P(AGE-co-EO) minority block. Stochastic optical reconstruction microscopy (STORM) of the resulting polymer—inorganic nanocomposite thin films shows nanodomain features of the two chemically dissimilar blocks consistent with atomic force microscopy results. This work paves the way for multiplexed OSRM analysis of polymer nanocomposite bulk structures.

he introduction of optical super-resolution microscopy (OSRM), a set of optical far-field imaging techniques for visualizing features below the diffraction limit of light, provides an intriguing opportunity for materials science. As a nanocharacterization tool, which is complementary to electron and scanning probe microscopies, OSRM offers a combination of capabilities including three-dimensional (3D), high-spatiotemporal resolution, and multicolor imaging in the nanometer regime, without the often stringent environmental requirements surrounding especially electron microscopy techniques (e.g., ultrahigh vacuum).1,2 While OSRM has generated thousands of polychromatic images of biological specimens, the corresponding multicolor optical imaging of abiotic nanoscale materials has remained challenging. This circumstance is due, in large part, to the lack of appropriate specific and orthogonal (i.e., with mutually incompatible chemical affinities) imaging probes that work in what is often the condensed state of multicomponent nanomaterials, which frequently lack the diverse reactivity and molecular recognition that typify biological samples in aqueous solution environments.² Self-assembled block copolymer (BCP) nanostructures, in particular as thin film nanopatterns, exemplify this challenge.^{3–8} As a result of their characteristic feature sizes on

the nanoscale, periodic order, dynamic self-assembly, and structural tunability, BCPs have served as a prototypical example for the application of OSRM in materials science. However, optical visualization in these materials has essentially been confined to single-color imaging of specific nanoscale structural features. ^{9–14} Here, we present a strategy that exploits differences in polarity and reactivity for orthogonal two-color labeling of the two nanodomains of model amphiphilic diblock copolymer thin films.

Stochastic optical reconstruction microscopy (STORM), a form of single-molecule localization microscopy (SMLM), is less demanding in terms of instrumentation requirements as compared to other OSRM approaches while still facilitating noninvasive tracking of dynamic processes like BCP self-assembly with reasonable temporal resolution. ^{1,15} To take full advantage of STORM's capabilities in multicolor BCP imaging,

Received: April 6, 2021 Revised: June 4, 2021



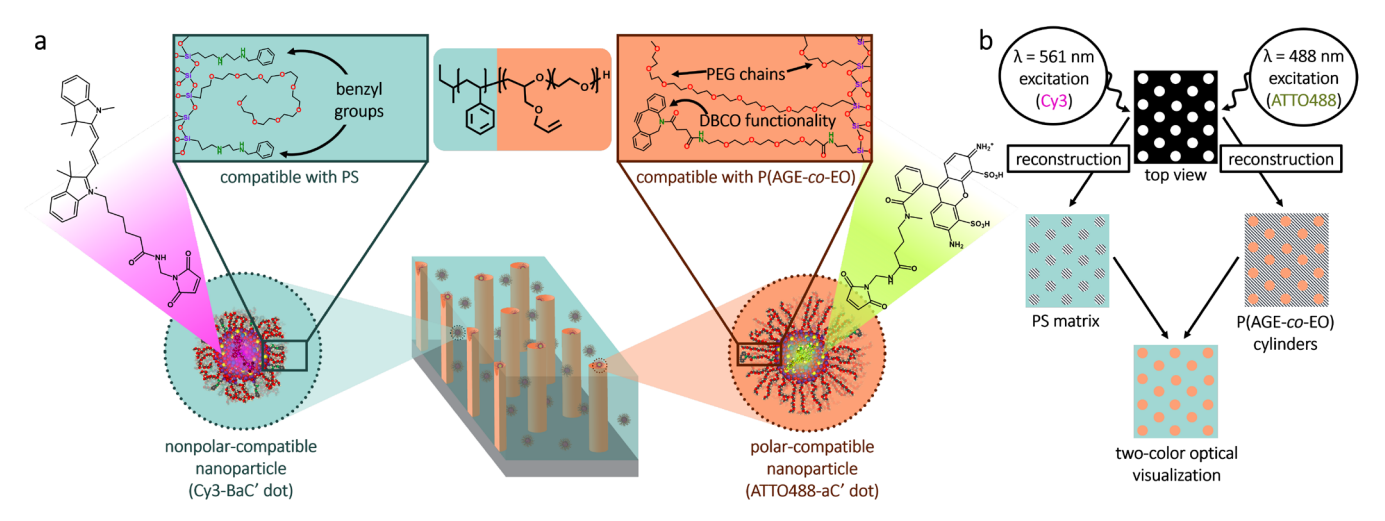


Figure 1. Schematic representations of compatibilization of orthogonal nanoprobes encapsulating different fluorescent dyes and with different surface characteristics for compatibilization with a chemically distinct BCP matrix or surface domains (a) and two-color optical super-resolution image reconstruction process (b).

precise orthogonal labeling^{1,2} of each block with highly selective nanoprobes—that is, compatibilization of fluorescing OSRM-enabling species with a specific polymer block domain-becomes a prerequisite. In aqueous biological systems, such specificity is often achieved by employing antibodies labeled with STORM-enabling dyes directed to, e.g., specific cellular target sites, together with imaging cocktails with blink-inducing agents that facilitate the appropriate dyeblinking behavior required for this OSRM. 16,17 Applying SMLM to abiotic materials systems in the condensed state, such as BCP thin-film nanostructures, produces an alternative set of criteria for orthogonal optical probes to achieve specific labeling, preferably by facile mixing or surface modification strategies. The development of such potent orthogonal OSRM probes for multicolor imaging has remained challenging, however, explaining the slow adoption of these exciting techniques in materials science. At the forefront of this dilemma is the ability to strategically compatibilize effective probes with appropriate material components (here: distinct BCP domains). Although prior work has assessed inducible emission and/or blinking in solid-state polycrystalline nanomaterials 19,20 or individual conjugated polymer molecules, 21 such systems take advantage, e.g., of autofluorescence atypical of many polymers. Such research has focused primarily on the characterization of photoluminescent behavior rather than on the application to SMLM. Thus, for further translation of OSRM to soft materials like polymers, there is a need for compatible optical probes that can selectively integrate into specific nanodomains for their visualization.

Chemical and physical compatibility proves essential to many fields and in many forms: ceramic- or electrolyte-compatible electrodes in solid-state batteries; ²², ²³ osmoprotectants; ²⁴ cell- or blood-compatible hydrogels, ²⁵, ²⁶ theranostic targeting, ^{27–30} and substrate design³¹ in biology; and solvent selectivity, ³², ³³ plastic—conductor integration, ³⁴ and effects on moisture diffusion ³⁵ in materials. Such preferential association is often only achieved with great difficulty; ^{36,37} thus, compatibilization of nanoprobes with largely unaccommodating polymer matrices like polystyrene (PS) is both desirable and challenging. ^{38,39} In the polymer community, the criteria for successful mixing of nanoparticles into BCP domains ^{40–42}

via nanoengineered particle surfaces have been under continuous investigation. 43–45 Ligand variations on gold nanoparticles, 46 lipophilic particles from aqueous conditions, 47 and one-pot syntheses of related hydrophobic materials 48,49 have all been reported. Not only does a compatibilization approach offer the convenience of facile sample preparation via mixing, but it also leads to polymer nanocomposites, which are interesting subjects of study in their own right. Postsynthesis PS or nanoparticle surface modification, 50,51 grafting via radical polymerization, 52–54 and emulsions and dispersions 43,55 have dominated such research into PS—particle nanocomposites. 66 While each of these modes of preparation has its own set of benefits and disadvantages, there is a clear lack of routes that enable compatibilization of nanoparticles that may further function as OSRM probes.

Here, using BCP-nanoprobe composite thin films as a model system, we demonstrate high-resolution, two-color OSRM imaging to visualize two-dimensional (2D) nanostructural features across several square-micrometers (Figure 1). This work makes use of ultrasmall (diameters below 10 nm), covalent dye-encapsulating aluminosilicate core—organic ligand shell (core-shell) nanoparticles. These aluminumcontaining probes synthesized in water are referred to as aluminosilicate Cornell prime dots (or simply "aC' dots"). 57 While we showed previously how to modulate the photophysical properties of aC' dots for STORM by modifying the nanoparticle core, in the present study we will instead focus on the chemistry of the ligand shell of these particles in order to compatibilize them with different polymer nanodomains. Careful design of their surface functionalities through tailored syntheses facilitates selective labeling of either of the two domains of a cylinder-forming diblock copolymer in thin films. Compatibilization is achieved in the nonpolar matrix domain via simple BCP-nanoprobe mixing before film formation or with the exposed polar cylinder domains, with pendant alkenes, via click chemistry-mediated surface attachment after film formation (Figure 1a). The faithful imaging of nanostructural features is affirmed by complementary atomic force microscopy (AFM). These organic-inorganic nanocomposites take advantage of dye-specific excitation/emission: Matrix- and surface-labeling probes can be distinguished by their color, i.e.,

their emission/absorption properties, enabling reconstructed overlays distinguishing the two domains with distinct colors (Figure 1b). To that end, the cores of the aC' dots encapsulate either Cy3 or Cy5 in a mixed poly(ethylene glycol) (PEG)/benzyl-bearing (PEGylated/benzylated, nonpolar-compatible) probe (benzylated PEG-Cy3/5-aC' dots) or ATTO488 in a PEGylated and subsequently alkyne-functionalized (polar-compatible and reactive) probe (PEG-ATTO488-aC' dots). These probes were then used as visualization tools in STORM. We envision that such ultrasmall modular and orthogonal core—shell nanoprobes, with colors defined by dye choice in the core and specific compatibility defined by tunable surface chemical properties of the shell, will expedite the pervasion of multicolor OSRM in multicomponent abiotic condensed-phase materials systems.

■ RESULTS AND DISCUSSION

Nanoprobe Design and Synthesis. We first synthesized regular PEG-dye-aC' dots and benzylated PEG-dye-aC' dots encapsulating Cy3 [555 nm/570 nm excitation/emission] and Cy5 [646 nm/662 nm excitation/emission] dyes, further abbreviated as Cy3- or Cy5-aC' dots and Cy3- or Cy5-BaC' dots, respectively.⁵⁸ After purification of as-synthesized materials via gel permeation chromatography (GPC, Figure S1), particle hydrodynamic size and dyes per particles were determined via fluorescence correlation spectroscopy (FCS, Figure S2) in combination with optical spectroscopy, as described elsewhere.^{57–59} The results summarized in Table 1

Table 1. Summary of Nanoparticle Probe Characteristics

nanoprobe	hydrodynamic diameter ^a (nm)	dyes per particle ^b	average BATMS per particle
ATTO488-aC' dots	5.5 ± 0.2	1.3	N/A
Cy3-aC' dots	4.4 ± 0.2	1.3	N/A
Cy3-BaC' dots	8.5 ± 0.1	1.6	~130
Cy5-aC' dots	6.2 ± 0.2	1.1	N/A
Cy5-BaC' dots	7.2 ± 0.3	1.5	~64

^aMeasured by FCS. ^bCalculated from FCS-derived concentrations together with absorbance data from optical spectroscopy.

show particle sizes below 10 nm and an average number of dyes per particle between 1 and 2 for all particles synthesized. Transmission electron microscopy (TEM) on the resultant particles (Figure S3) affirms the small particle sizes suggested by fits of FCS correlation curves as well as GPC results.

As recently studied in detail, in these particles blinking is due to an aluminum-mediated redox mechanism that enables switching between fluorescing "on" and long-lived dark or "off" states. ⁵⁷ In this way, blinking can be induced by a single excitation source/laser and in the absence of special imaging buffers typically required to enable STORM, greatly simplifying image acquisition. This blinking mechanism is distinctly different from one described in an earlier study on thiol-containing super-resolution Cornell prime dots or srC' dots. This earlier study involved two lasers for light-induced formation and subsequent cleavage of a thiol adduct that disrupts electron delocalization along the dye's carbon backbone using thiol groups co-condensed into the aluminosilicate particle core. ⁵⁹

To enable compatibilization of these particles with different nanodomains of BCPs, the fluorescent aluminosilicate cores need to be functionalized with an organic shell. In previous work, we demonstrated that hydrogen bonding enables fast adsorption and subsequent covalent attachment of PEG-silane groups (PEGylation) to the surfaces of silica-based C' dots and aluminosilicate-based aC' dots during their one-pot synthesis in water as the reaction medium. 58 These rapid attachment (PEGylation) kinetics accelerate the transition through the "valley of death" between electrostatic and steric nanoparticle stabilization. The work herein presented relies on the postulation that it should be possible to translate the same principles to the formation of a mixed surface coating: a pseudo-PEGylation using additional silanes with a backbone consisting of secondary amines in place of ethers. Thus, the hydrogen bonding that enables fast adsorption of PEG to the aluminosilicate surface in water could be translated to that of multiple amino groups. With these criteria in mind, N-(2-Nbenzylamino-ethyl)-3-aminopropyl-trimethoxy-silane (BATMS, molecular structure in Figures 1a and 2) was selected as a surface ligand in order to introduce hydrophobic benzyl groups to the aC' dot surface in an effort to compatibilize these particles with PS BCP domains. More broadly, Figure 2 delineates the aqueous synthesis steps of our benzylated BaC' dots for OSRM imaging.

Two primary deviations from previously published super-resolution aC' dot^{57,59,60} synthesis protocols enabled an aqueous one-pot approach to such particles with hydrophobic BATMS moieties for compatibilization with PS (Figure 2). First, the immediate addition of BATMS subsequent to 2-[methoxy(polyethyleneoxy)₆₋₉(propyl)] trimethoxysilane ("PEG₆₋₉-silane") allowed for simultaneous particle stabilization via PEGylation and incorporation of pendant hydrophobic benzyl groups into the organic ligand shell. Despite the benzyl group, through increased hydrogen bonding strength between the secondary amines of BATMS and silica surface silanol groups (Figure S4), coupled with the relatively short ligand length, the affinity of BATMS to the silica surface is expected to be higher than that of the PEG ligands. Even though PEG₆₋₉-silane was added first, the BATMS was therefore expected to find its way between the PEGs to the aluminosilicate surface, where in aqueous solutions it can effectively hide from the hydrophilic environment.⁶¹

Second, the subsequent heating step, which is typically conducted at 80 °C, was decreased to 40 °C. Under aqueous conditions, the strength of hydrophobic interactions among the pendent groups of BATMS is expected to be high.⁶² The reduced heating temperature mitigated the hydrophobic effect among the benzyl groups during synthesis while still providing adequate energy to break H-bonds to complete the two-step PEGylation mechanism studied in detail earlier (step 1: hydrogen bonding to surface, step 2: condensation).⁵⁸ Figure S4 indicates the relative strengths of relevant hydrogen bonding pairs during synthesis. 61,63,64 To promote distribution of BATMS throughout the shell, disfavor particle aggregation, and reduce displacement of slightly weaker silanol hydrogenether oxygen interactions, we chose a PEG₆₋₉-silane/BATMS mole ratio of 5:1. The favorable competition by BATMS for Hbonding with surface silanol groups was thus compensated for through an excess of PEG₆₋₉-silane as well as the order of addition.

Investigations into inorganic nanoparticle compatibilization with hydrophobic domains have illustrated the significance of chain areal density, ⁶⁵ surface ligands, ⁶⁶ and nanofiller size ⁶⁷ on dispersion. The synthesis of BaC' dots consistently provided

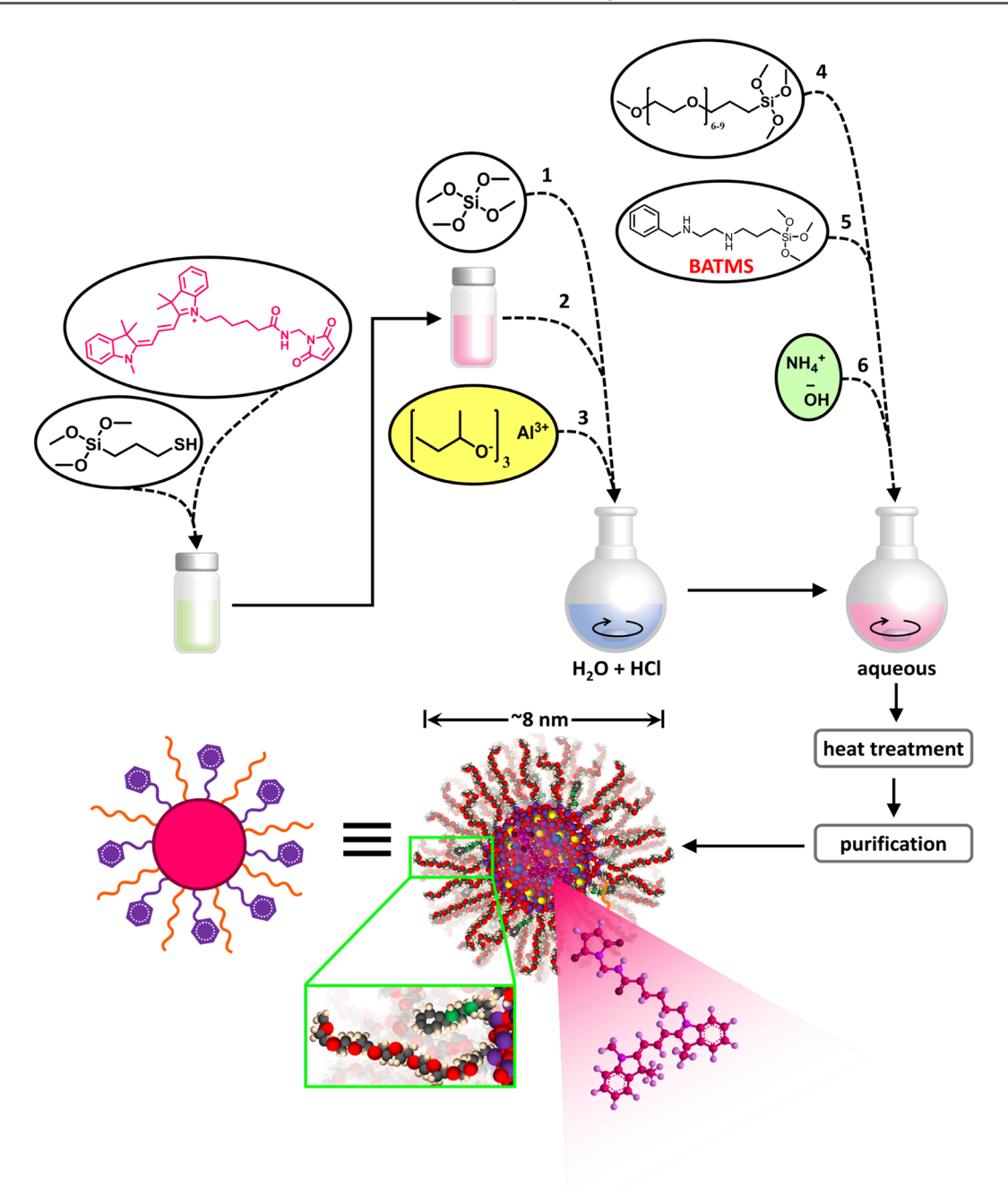


Figure 2. Reaction scheme for the preparation of Cy3-BaC' dots. Cy3-maleimide dye (magenta) is combined with (3-mercaptopropyl) trimethoxysilane (MPTMS) in dimethyl sulfoxide (DMSO). Tetramethyl orthosilicate (TMOS), the dye–silane conjugate solution, and aluminum-tri-sec-butoxide (ASB) in 2-propanol (IPA) are sequentially added to a stirring HCl(aq) solution. Shortly thereafter, PEG₆₋₉-silane and BATMS are added in swift sequence. Several minutes later, H_2O/NH_4OH is added to rapidly raise the solution pH. The following day, the solution is removed from stirring and heated at 40 °C for 24 h. The particles are up-concentrated and purified using GPC before characterization.

high loading of benzyl groups, as suggested by UV-vis absorbance measurements. Figure S5 shows concentration-dependent absorbance spectra of BATMS in ethanol exhibiting three characteristic shallow peaks between 250 and 270 nm. Using these data, we determined three BATMS extinction coefficients (Figure S5a-d). Comparison with UV-vis absorbance spectra of BATMS-functionalized BaC' dots (Figure S5e,f) clearly confirmed the presence of this ligand on the particle surface. Using the extinction coefficients and neglecting solvent effects, by averaging results obtained from the three different wavelengths (see Table S1) we estimated the number of BATMS groups from the absorbance data in

water as ~130 or ~64 per Cy3- or Cy5-BaC' dot, respectively. These values can be compared with results of our previous work on the number of PEG chains on regular C' dots. S8,68 Nanoparticles with silica core radii of 1.8 nm were estimated to have ~70 PEG chains on their surface with an estimated density of 1.7 PEG chains/nm² in brush-like conformations. Assuming a PEG layer thickness of around 1 nm, as derived from recent form-factor analysis of synchrotron-based small-angle X-ray scattering experiments on C' dots, FCS-derived hydrodynamic core radii of BaC' dots can be estimated as 3.2 and 2.6 nm for Cy3- and Cy5-BaC' dots, respectively. These values translate to an estimated aluminosilicate core surface

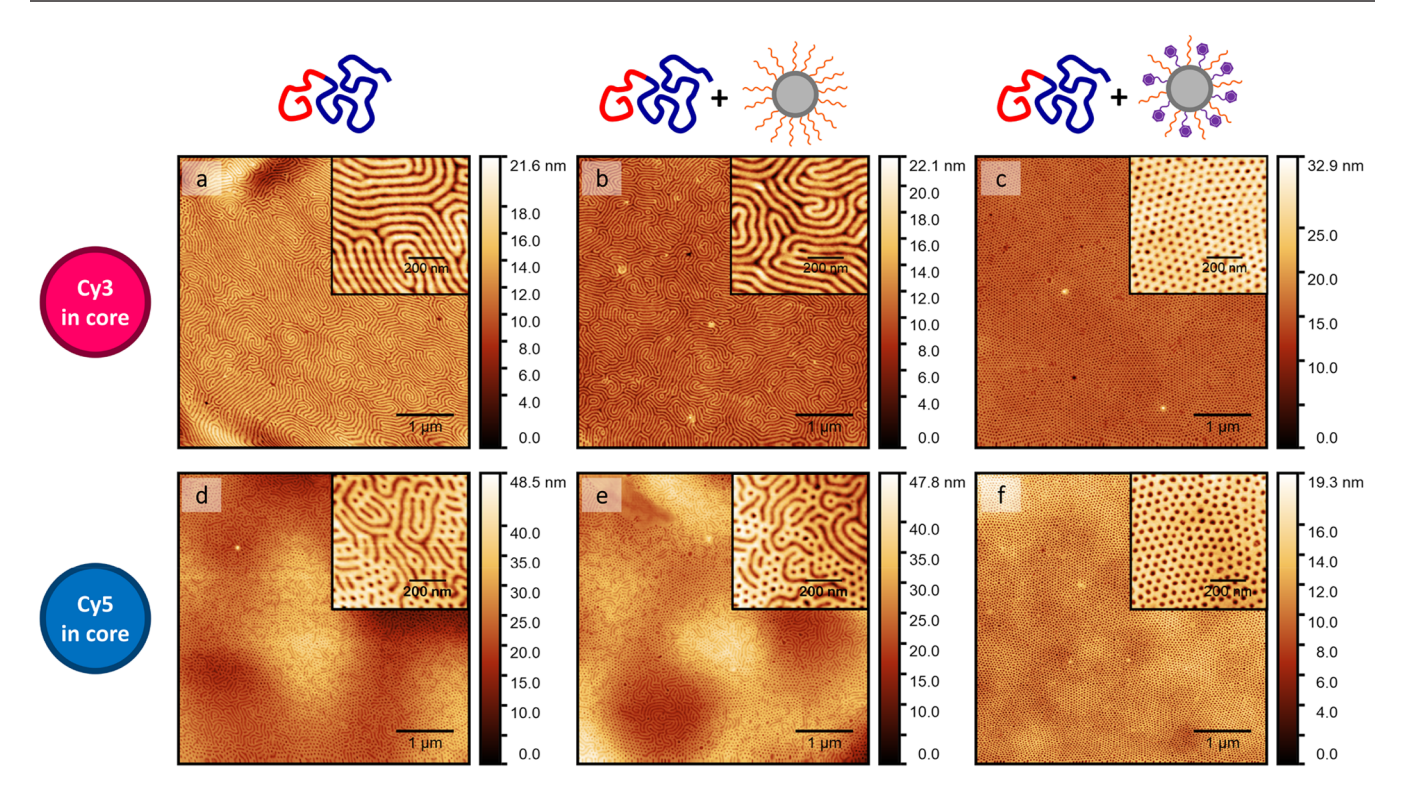


Figure 3. Dry-state AFM height images comparing PS-*b*-P(AGE-*co*-EO) films prepared without additive (a, d) with corresponding nanocomposite films prepared with Cy3-aC′ dots (b), Cy3-BaC′ dots (c), Cy5-aC′ dots (e), and Cy5-BaC′ dots (f). Insets show representative images at a higher magnification.

area roughly three times or twice as large as the original C^\prime dots for Cy3- and Cy5-Ba C^\prime dots, respectively. Assuming for simplicity that PEG density is independent of particle size leads to an estimated 230 and 140 PEG chains per particle in the case of only PEGylated Cy3- and Cy5-Ba C^\prime dots, respectively.

Comparison of these PEG chain estimates with the measured BATMS numbers of \sim 130 and \sim 64 for the same particles suggests that despite the 1:5 mole ratio between BATMS and PEG-silanes in the synthesis feed and the sequence of addition in which BATMS is added into the synthesis reactor shortly after the PEG₆₋₉-silane, BATMS groups have greater affinity for the particle surface than the PEG-silanes. This observation in turn is consistent with our foregoing discussion about the smaller size and the increased H-bonding strength of the BATMS ligand as compared to PEG₆₋₉-silane ligand (see Figure S4), which favor a combination of partial displacement of PEG₆₋₉-silane by BATMS and insertion of BATMS between PEG ligands.

Preparation of Nanocomposite Thin Films for OSRM. We have previously shown that ultrabright aluminosilicate probes can undergo selective covalent attachment via "click" chemistry to pendant alkene groups in the polar domain of a functional BCP with a majority PS block, polystyrene-block-poly[(allyl glycidyl ether)-co-(ethylene oxide)] or PS-b-P(AGE-co-EO). This approach enabled nanoscale imaging of BCP thin film surfaces using STORM. In order to maximize the value of SMLM techniques like STORM as a nanocharacterization tool complementary to electron and scanning probe microscopies, the development of orthogonal nanoprobes enabling two-color OSRM imaging of the two domains of such diblock copolymers is highly desirable. The lack of a reactive functional group in the PS block of PS-b-P(AGE-co-EO) suggested physical mixing of fluorescent

nanoprobes throughout the PS block as a viable strategy. We used the benzylated BaC^\prime dots for selective compatibilization with, and OSRM imaging of, the PS block. 1,56

The model PS-b-P(AGE-co-EO) BCP with molar mass $M_n =$ 75 600 g mol⁻¹, polydispersity D = 1.11, volume fraction $f_{PS} =$ 0.76, and AGE/EO ratio 1:4 was synthesized using anionic polymerization and in thin films showed P(AGE-co-EO) cylinders in a PS matrix (Figure 3), all as previously reported. Nanoparticle–BCP composite thin films were generated by spin-coating mixed particle-polymer solutions in benzene onto silicon wafers, followed by solvent vapor annealing (SVA) and drying (see Experimental Section). The expectation was that the benzylated aC' dots would be nonpolar enough and have sufficiently small core diameters to fully mix with the PS block of PS-b-P(AGE-co-EO) without segregating out.⁷² Figure 3 shows AFM images of parent BCP (a, d) and nanocomposite films obtained from adding regular PEGylated Cy3- or Cy5-aC' dots (b, e) and benzylated Cy3or Cy5-BaC' dots (c, f) to the BCP solution for spin-coating. While regular PEGylated particles did not have any substantial effects on resulting film morphologies (compare Figure 3a,d with Figure 3b,e), adding benzylated particles changed the film surface structure away from lying-down cylinders to hexagonal patterns with standing-up cylinders (see Figure 3c,f). This observation was accompanied by an increase in domain spacing. For example, based on 40 randomly selected cylinder pairs (in regions with hexagonal local order), the cylinder-tocylinder distance increased from 50.5 \pm 6.5 nm to 54.8 \pm 3.9 nm when moving from parent BCP to Cy5-BaC' dotscontaining composite films (Figure 3d,f). This behavior is consistent with preferential swelling of PS blocks by BaC' dots.32,73,74

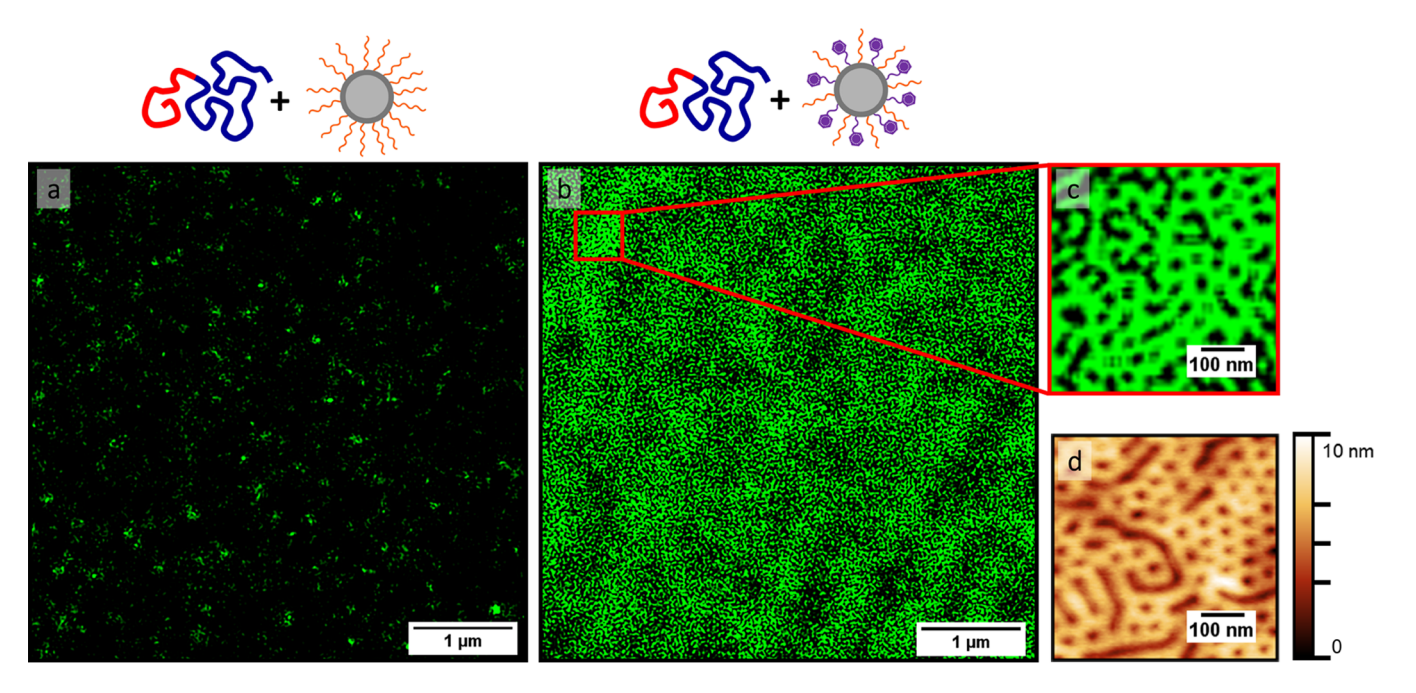


Figure 4. STORM images of nanocomposite films prepared using Cy3-aC' dots (a) and Cy3-BaC' dots (b). Region of interest from (b) at higher magnification (c) compared to an AFM image taken at the same scale (d).

Single-Color OSRM Imaging of BCP Composite Thin Films Using STORM. Preferential swelling of PS domains by our BaC' dots was corroborated by OSRM imaging of these BCP thin-film composites. STORM reconstructions were obtained from images of nanocomposite films taken in the total internal reflection fluorescence (TIRF) microscopy mode (see Experimental Section). Due to the sub-10 nm diameters, particle Rayleigh scattering at the wavelengths employed is negligible.⁷⁵ Figure 4 compares resulting STORM images of BCP nanocomposite films from Cy3-aC' dots (Figure 4a) with those of Cy3-BaC' dots (Figure 4b). While, in the case of regular Cy3-aC' dots, the fluorescence signal is sparse due to lack of significant incorporation into either block, in films prepared with the benzylated Cy3-BaC' dots the entire 5×5 - μ m² area of the film shows strong fluorescence signal consistent with BCP nanostructure. Focusing on one region of the latter film at higher magnification reveals a BCP morphology with a mix of lying-down and predominantly standing-up cylinders with the fluorescence signal coming from the majority (i.e., PS) domain, similar to what is observed for this film on the same length scale with AFM (compare Figure 4c,d). These results together suggest that the simple mixing strategy of STORM probes with the PS-b-P(AGE-co-EO) BCP allows successful reconstructions of the BCP surface nanostructure via selective swelling of the PS domains by BaC' dot probes. They further prove encouraging with respect to morphological identification of BCP mesostructure using SMLM alone, i.e., without the need for corroborative AFM, as has been demonstrated using stimulated emission depletion microscopy (STED).4

The domain spacings measured by AFM and STORM are nearly identical (46.4 ± 3.7 nm and 46.8 ± 5.0 nm, respectively) for the same set of samples (i.e., prepared under the same conditions at the same time), providing further evidence that the nanoparticles are incorporated into the matrix and not isolated at the film surface. These cylinder-to-cylinder distances are well within the lateral resolving

capabilities of both AFM and SMLM, 76 whose correlative use has been on the rise in biology. 77 More specifically, Cy3-aC' dots generated on average 30 100 photons per localization event (see Figure S6), which translates to a mean localization uncertainty of 7.2 \pm 1.1 nm. These values are remarkably consistent with those reported for Cy3-srC' dots, 60 corroborating earlier studies that enhanced fluorescent behavior (over free dyes) is preserved despite the core compositional differences between aC' and srC' dots. 57

From previous studies of hydrophilic/polar compatibilization in BCPs, if particle diameter exceeds the radius of gyration (R_{σ}) of the desired block for mixing, then it is expected that particles segregate out based on entropic factors, even if the enthalpy favors mixing.^{72,78} The absence of this segregation phenomenon in our experiments warrants a look at other factors dominating the behavior of our BaC' dots in the nonpolar PS block of the PS-b-P(AGE-co-EO) di-BCP.⁶⁷ The hydrodynamic diameters of the Cy3- and Cy5-BaC' dots are 8.5 ± 0.1 nm and 7.2 ± 0.3 nm, respectively. The freely jointed chain model (see Equation S1) approximates R_q of the PS block in the BCP used here as ~7.2 nm, i.e., at or slightly below the particle sizes. While the preparation of our nanocomposites in benzene (i.e., a good solvent for PS) would render this calculation an underestimation in solution (see Equation S2),³³ a more likely explanation is that enthalpic effects dominate the behavior observed in our thin films, which can offset entropically driven (i.e., size-dependent) repulsion when nanoparticle surface chains are sufficiently compatible with this polymer matrix.⁷⁹ The R_g of the P(AGE-co-EO) block, on the other hand, is estimated as only 4.1 nm. This value, which is smaller than the diameters of our Cy3- and Cy5-aC' dots, explains why the polar aC' dots do not selectively incorporate into the minority domain by simple physical mixing (i.e., they tend toward entropic segregation). This further motivated our use of click chemistry to covalently attach our probes to the surface of the P(AGE-co-EO) cylinders.

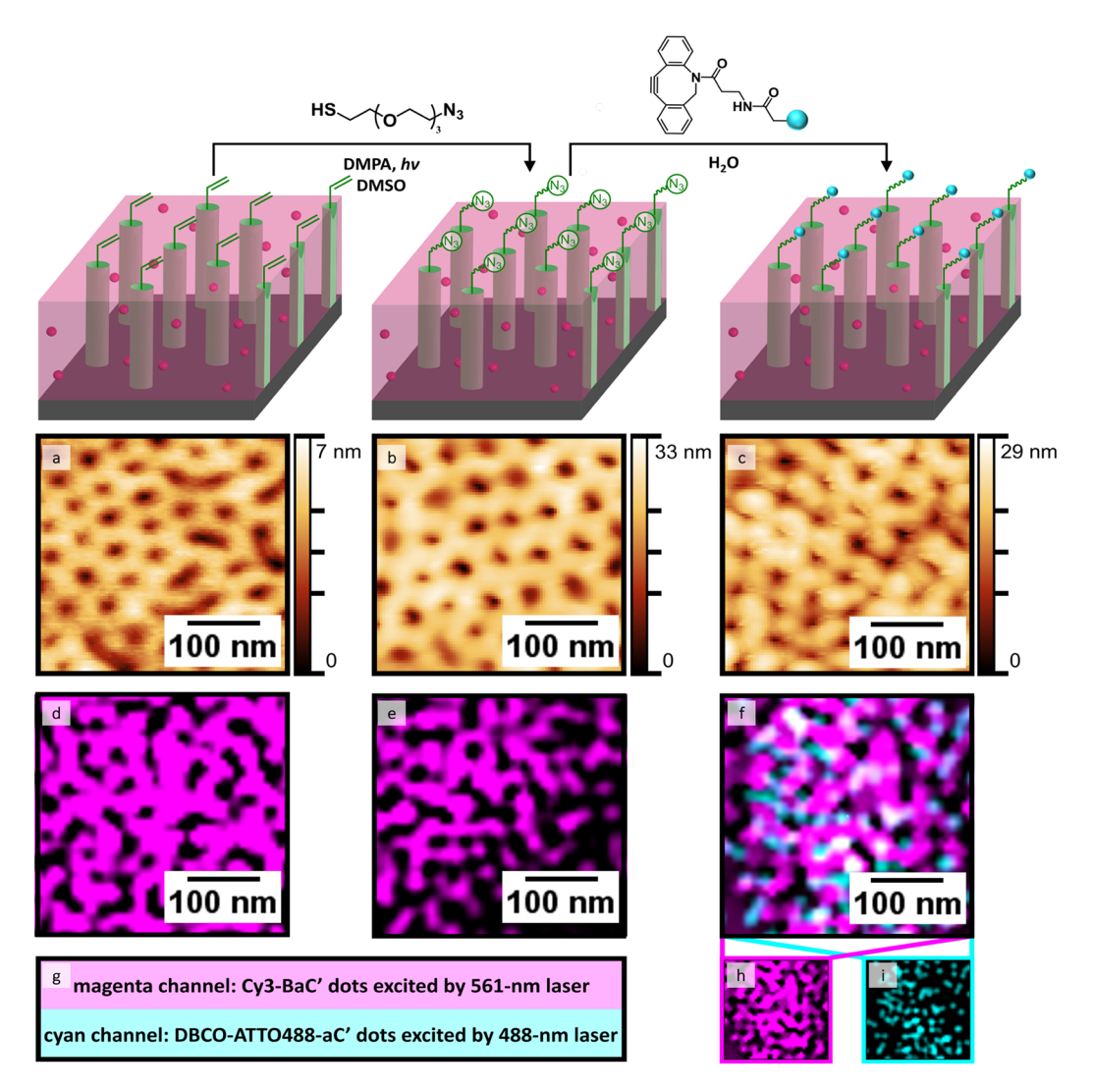


Figure 5. Top: Scheme showing the initial nanocomposite film, surface functionalization of the hydrophilic domain with azides, and subsequent attachment of ATTO488-aC' dots above the respective data sets for each experimental step. AFM height (a-c) and STORM (d-f) images of the parent nanocomposite (Cy3-BaC') dots in PS-b-P(AGE-co-EO) film (a,d), film functionalized with azide (b,e) using click chemistry, and film that has undergone both surface functionalization with azide and subsequent attachment of ATTO488-aC' dots (c,f) demonstrating mesostructure preservation (e) upon postassembly processing and successful two-color OSRM imaging (f) of the two distinct BCP domains. Legend (g) for single-color false-magenta (h) or -cyan (i) channels merged to generate the two-color image in (f).

Previous attempts at tuning particle surface polarity for incorporation into PS-b-poly(2-vinylpyridine) noted that alkylated gold nanoparticles may associate with PS after nonequilibrium spin-coating but migrate to the more polar block upon SVA. 66 In contrast, even after a 20-h SVA step in benzene, our BaC' dots appeared to stay in the PS domain, suggesting durable compatibility. Lastly, it has been demonstrated that even gold nanoparticles with high hydrophobic content in mixed-ligand shells can be soluble in water, 46 consistent with both of our observations that the BaC' dots are soluble in aqueous solutions as well as in nonpolar polymer environments.

The observed selective swelling of the PS domains by BaC' dots and lack of segregation even after extended SVA times may be due not solely to the presence of the BATMS ligands on the particle surface but also to contributions from the PEG ligands. The favorable enthalpic interaction between PS and poly(vinyl methyl ether) (PVME) is well documented in the field of polymer blends. 80,81 This surprising phenomenon is

attributed exclusively^{82,83} to molecular-level interactions between nonbonding electrons on PVME's ether oxygens and the delocalized π -electron system of the phenyl rings of PS. This effect likely translates to the BaC' dots: As with the COCH₃ groups of PVME, ⁸⁴ there are likely favorable enthalpic interactions between ether oxygens in PEG and phenyl rings in PS. It is worth noting, however, that purely PEGylated particles do not associate with the PS matrix in the BCP. While the presence of PEGs may lend a degree of enthalpic favorability to help facilitate compatibilization (and allow for straightforward aqueous nanoparticle synthesis), the benzyl-capped groups from BATMS are required to (i) induce the observed compatibility with PS blocks and (ii) prevent compatibility of the BaC' dots with the P(AGE-co-EO) block of the BCP studied here. Finally, the PS-b-P(AGE-co-EO)-BaC' dot nanocomposite thin films were prepared in benzene, which has been shown to promote miscibility of PVME and PS,85 and well below the PS-PVME system's lower critical solution temperatures^{80,81} for relevant molar masses.

Two-Color OSRM Imaging of BCP Composite Thin Films Using STORM. Simply mixing BaC' dots into the PS matrix left the allyl surface groups of the P(AGE-co-EO) block domains of PS-b-P(AGE-co-EO) available for orthogonal attachment of a second, differently colored aC' dot to the thin BCP film surface, thereby enabling two-color OSRM imaging of the two domains of di-BCP nanostructures. To that end (see schematic in Figure 5, top row), the nanocomposite films underwent "click" chemistries, as per our earlier reported protocol, 60 first using thiol-ene click chemistry to attach an $\alpha_{1}\omega$ -functionalized PEG, i.e., thiol-PEG₃-azide, to the film surface. This reaction was followed by a strain-promoted alkyne-azide click reaction with dibenzocyclooctyne (DBCO)-functionalized PEG-dye-aC' dots. This treatment selectively attached DBCO-functionalized ATTO488-aC' dots to free AGE moieties on the BCP thin film surface, which should therefore be confined to the cylinders of the polar

Figure 5 exhibits AFM height images (a-c) and STORM reconstructions (d-f) of a parent nanocomposite (Cy3-BaC' dots in PS-b-P(AGE-co-EO)) film (a, d), the same nanocomposite film after functionalization with azide via thiol-ene click chemistry using thiol-PEG3-azide (b, e), and the final resulting film that underwent further surface attachment via strain-promoted alkyne-azide click chemistry with DBCOfunctionalized ATTO488-aC' dots (c, f). The AFM images show nanostructure preservation upon postassembly processing. The single-false-color STORM images show parent (d) and azide-functionalized (e) films, as well as the two-false-color STORM image (f) of the final resulting nanocomposite film with Cy3-BaC' dots mixed into the nonpolar PS matrix domains and functionalized ATTO488-aC' dots covalently confined to the polar P(AGE-co-EO) domain surface. Small overlapping regions in Figure 5f are likely the result of the limited mobility associated with surface-attached nanoparticle probes, as described previously. ⁶⁰ Nevertheless, these images demonstrate proof-of-principle of the successful visualization, in the far-field regime of an optical microscope, of both of the two nanoscopic domains of the diblock copolymer via two distinctly colored orthogonal probes. While presented here as a complement to AFM, such chemical distinction of unique structures on the mesoscale lends credence to STORM's potential as a standalone polymer characterization tool, as mentioned earlier. Exploration of this research avenue necessitates further optimization of probe distribution, however, to maximize optical coverage of each desired block.

CONCLUSION

In summary, this work has achieved two notable advances. The first is a facile aqueous synthesis protocol for the preparation of PS-compatible, ultrasmall OSRM imaging probes (BaC' dots) that may be added to nonpolar BCP domains via simple solution mixing. The second is their use together with a second set of orthogonal probes "clicked" onto the BCP film surface for two-color OSRM imaging of the two distinct nanodomains of a di-BCP thin film nanocomposite nanostructure. For optical imaging, a TIRF microscopy geometry was chosen to enhance signal-to-noise ratios. Since such setups require the use of a thin water layer between the imaging cover glass and thin-film surface, covalent linkage of the second probe to the polar BCP domain was helpful in preventing probe leaching. It should be noted, however, that moving away from the TIRF geometry toward, e.g., spinning-disc confocal microscopy

(SDCM) setups for STORM would remove the requirement of the presence of water. ^{86,87}

The results presented here, which demonstrate successful and robust physical mixing of an aqueously synthesized OSRM probe into the nonpolar PS domain of an amphiphilic BCP, may open up a pathway to two-color STORM imaging of the two domains of such microphase-separated polymer systems based entirely on simple mixing strategies. Our previous work has shown that, facilitated by dipole-dipole, hydrogenbonding, or screened electrostatic interactions, it is relatively straightforward to successfully compatibilize ultrasmall nanoparticles with hydrophilic/polar domains of phase-segregated BCP systems. 37,72 Using two tunable and orthogonal (i.e., encapsulating two different dyes and with either polar or nonpolar surface coatings), ultrasmall aC' dot and BaC' dot probes may enable facile labeling and STORM imaging strategies, in the absence of a second laser and complex imaging buffers. Simply mixing both of these probes together with the microphase-separating block copolymer in solution would then enable preparation of the final nanocomposite film samples. Future studies could explore local-field mapping in solid-state polymers, akin to related studies using single molecules to probe local properties in polycrystalline materials. 88,89 This research could then find ready application in optical characterization and probing, e.g. of polymer blends in hybrid or fully organic solar cells. 90 It will be interesting to see whether the work presented here as well as additional analogous strategies will help to further popularize OSRM imaging techniques in the polymer community, in particular toward the multiplexed OSRM imaging of nanocomposites in the bulk at length scales below the diffraction limit of light.

■ EXPERIMENTAL SECTION

Materials. Benzene (anhydrous, 99.8%) and methanol (anhydrous, 99.8%) were purchased from Krackeler Scientific, Inc. Dimethyl sulfoxide (DMSO), 2-propanol (IPA, anhydrous 99.5%), aluminum-tri-sec-butoxide (ASB), (3-aminopropyl) triethoxysilane (APTES), ammonium hydroxide solution (28.0-30.0% NH₃ basis), (3-mercaptopropyl)trimethoxysilane (MPTMS), tetramethyl orthosilicate (TMOS), and 2,2-dimethoxy-2-phenylacetophenone (DMPA, 99%) were purchased from Sigma-Aldrich. Thiol-PEG3-azide was purchased from Conju-Probe, LLC. Cy3- and Cy5-maleimide dyes were purchased from Lumiprobe Corporation. 2-[Methoxy-(polyethyleneoxy)₆₋₉(propyl)]trimethoxysilane, hereafter referred to as PEG₆₋₉-silane, and N-(2-N-benzylamino-ethyl)-3-aminopropyltrimethoxysilane (BATMS) were purchased through Gelest, Inc. All chemicals were used as received. Deionized (DI) H_2O at 18.2 $M\Omega$ ·cm was generated with a Millipore Milli-Q system. Boron-doped (100) silicon wafers were purchased through WRS Materials. NanoWorld NCH-10 AFM tips were purchased from NanoAndMore USA Corporation.

Aqueous Synthesis and Characterization of BaC' Dots. The sequential processes depicted in Figure 2 comprise the one-pot aqueous synthesis of our BaC' dots. A total of 48.8 μ L of 0.005-g mL⁻¹ Cy3-maleimide dye, 51.2 μ L of DMSO or 9.4 μ L of 0.025-g mL⁻¹ Cy5-maleimide dye, and 90.6 μ L of DMSO were combined with 1.58 μ L of MPTMS in a 1.5-mL centrifuge tube and allowed to conjugate for 5 h. A total of 9.6 mL of fresh deionized (DI, 18.2 MΩ-cm) water and 400 μ L of HCl (0.500 normal) were added to a clean 25-mL round-bottom flask and allowed to stir for ~15 min. The following were added quickly in sequence to the stirring aqueous HCl solution: 78 μ L of TMOS, all of the conjugated dye, and 200 μ L of 1:9 (v:v) ASB/IPA solution (caution: ASB reacts violently with water). After 15 min, 125 μ L of PEG₆₋₉-silane was added to the stirring solution, followed immediately by 15.5 μ L of BATMS for a PEG₆₋₉-silane/BATMS mole ratio of 5:1. After ~5 min, the pH of the

stirring solution was rapidly increased by adding 280 μL of 1:1 (v:v) $H_2 O/N H_4 OH$. A rubber septum was folded over the flask, the flask was covered with aluminum foil, and the solution was left to stir for 18 h. The solution was removed from stirring and heated at 40 $^{\circ} C$ for 24 h. The particle solution was up-concentrated at least three times using GE Healthcare Vivaspin MWCO 30 kDa centrifuge spin filters and subjected to gel permeation chromatography (GPC) using a BioLogic LP system and 275-nm UV detector. The particles were run through a column containing Sephacryl S-300 High Resolution resin from GE Healthcare with a 0.9-wt % NaCl aqueous solution at least once. The particles were characterized using UV—vis absorbance and fluorescence correlation spectroscopy (FCS) to determine hydrodynamic radius, particle concentration, amount of dye per particle, and average number of benzyl groups on each particle.

Preparation of BCP Thin Films. PS-b-P(AGE-co-EO) with molar mass $M_n = 75\,600 \text{ g mol}^{-1}$, polydispersity D = 1.11, volume fraction $f_{PS} = 0.76$, and 1:4 AGE/EO ratio was synthesized using anionic polymerization as previously reported.⁷¹ Solutions of 1.28- to 1.31-wt % of PS-b-P(AGE-co-EO) in benzene (with [BaC' dot] = 250 nM, for PS-nanoparticle nanocomposite films) was prepared by simply mixing together the constituents and stirring for 3 h before spincoating onto cleaned silicon wafers for 30 s at 3000 rpm. The films were transferred to a glass dish with a well of benzene and covered with a glass dome to generate a benzene-saturated atmosphere for a 20-h SVA step. The films were dried for at least 1 h prior to AFM or optical imaging. It should be noted that TIRF microscopy data were not collected on films prepared using Cy5-aC' dots or Cy5-BaC' dots due to persistent spherical aberrations from the optical interaction between the silicon substrate and the red laser. Additionally, relative humidity and room temperature were not controlled and therefore may have been different between the two series in Figure 3 (a-c versus d-f), which likely accounts for the small morphological differences observed between Figure 3a and Figure 3d (parent BCP films).

Surface Modification of BCP Thin Films. In a nitrogen glovebox, the Cy3-BaC' dot-BCP nanocomposite film was added to a solution of 10 mL of DMSO + 0.09 mL of 10-wt % thiol-PEG₃-azide in DMSO with [DMPA] = 2.5 mM. The solution was then agitated under 365-nm UV light for 8 h, after which the film was rigorously rinsed four times using DI water. After drying, the film was transferred to an aqueous solution of [ATTO488-aC' dots] = 100 nM, where the ATTO488-aC' dots were synthesized⁵⁷ and DBCO-functionalized⁵¹ as reported previously, which was then sparged using nitrogen for 15 min and subsequently agitated in darkness for 1 h. The film was removed and again washed four times with DI water.

AFM Imaging. All AFM data were obtained in air under ambient conditions with a Digital Instruments MultiMode scanning probe microscope (SPM) in tapping mode with 512 lines at 512 pixels/line (for each image) and a scan rate of 1.2 Hz. The manufacturing specifications of the uncoated silicon NanoWorld Standard Tapping Mode AFM Probes included an average tip radius of <8 nm, a force constant range of 21 to 78 N m⁻¹, and a resonance frequency range of 250 to 390 kHz.

Acquisition of TIRF Data. All data were acquired using a homebuilt microscope in TIRF geometry at room temperature. Films were placed face-down onto glass into steel well plates filled with 1 mL of DI H₂O. A 100× oil-immersion objective was used, along with an additional 1.6× lens (100 nm/pixel), to collect 10 000 frames with an exposure of 30 ms/frame, autofocus every 500 frames, and a gain of 200. Cy3-encapsulating aC′ dots or BaC′ dots were subjected to a green laser. For more comprehensive optical characterization of the core, see previous work on blinking statistics⁵⁷ and improvements (over fluorescent dyes upon encapsulation) in localization uncertainty based on fitting to a Gaussian point-spread function. Moreover, encapsulation restricts dye mobility, which assists in enhancing dye brightness and photostability relative to free dye, e.g., in aqueous solution.

For nanocomposite films with two different dye-encapsulating nanoparticles (Cy3-BaC' dots in the PS matrix and DBCO-functionalized ATTO488-aC' dots on the surface of the P(AGO-co-

EO) block, see Figure 5), the films were first exposed to the green laser (561 nm) to excite encapsulated Cy3 dye followed by the blue laser (488 nm) to excite encapsulated ATTO488 dye. This sequential approach allowed for data collection over the same surface region without bleaching the Cy3-BaC′ dots with the higher-energy laser. To optimize optical visualization, data for Cy3-aC′ dots or -BaC′ dots were collected using a tetramethylrhodamine isothiocyanate (TRITC) filter set (filter window: excitation/emission 532–554 nm/570–613 nm), while data for ATTO488-aC′ dots were collected using a fluorescein isothiocyanate (FITC) filter set (filter window: excitation/emission 467–498 nm/513–556 nm).

STORM Image Reconstruction. Per our previously published protocol, ⁶⁰ data from TIRF imaging were subjected to Thunder-STORM, ⁹² an ImageJ plugin. The visualization was based on a Gaussian PSF model and was processed with a lateral uncertainty of 10.8 nm, molecule localizations based on local maxima, 4-neighborhood connectivity, and an intensity range of 500–2500 photons. Proximal information for comparative purposes was extracted from reconstructed STORM images obtained from ImageJ.

Localization Analysis. Cy3-BaC' dots underwent biotinylation, dilution, and immobilization on streptavidin-coated glass dishes according to our published protocol. ^{57,93} For these separate experiments, we synthesized a new batch of Cy3-BaC' dots with hydrodynamic diameters of 7.1 ± 0.2 nm, ~ 1.5 dyes per particle, i.e., similar to the original batch described in Table 1. Immobilized nanoparticles of this batch were subjected to the green laser for $10\,000$ frames at 50-ms exposure. Per our previously established methodology, ⁶⁰ which equates localization uncertainty to the full-width at half-maximum of a Gaussian profile, ⁹⁴ localizations were fit to a Gaussian distribution (here: "Gauss" function in OriginPro), from which localization uncertainties were derived. A set of custom-built MATLAB codes compiled these data into a photon histogram and calculated the mean number of photons generated per localization event.

ASSOCIATED CONTENT

Supporting Information

The Supporting Information is available free of charge at https://pubs.acs.org/doi/10.1021/acs.chemmater.1c01204.

Calculation methods for radii of gyration, extinction coefficients, and quantification of BATMS groups; additional characterization data from GPC, FCS, TEM, and UV—vis absorbance; and scheme of relative H-bonding strengths (PDF)

AUTHOR INFORMATION

Corresponding Author

Ulrich B. Wiesner — Department of Materials Science and Engineering, Cornell University, Ithaca, New York 14853, United States; orcid.org/0000-0001-6934-3755; Email: ubw1@cornell.edu

Authors

I

Dana V. Chapman – Department of Materials Science and Engineering, Cornell University, Ithaca, New York 14853, United States; © orcid.org/0000-0002-9605-1886

Joshua A. Hinckley — Department of Chemistry and Chemical Biology, Cornell University, Ithaca, New York 14853, United States; Present Address: (J.A.H.) Koch Institute for Integrative Cancer Research, Massachusetts Institute of Technology, Cambridge, Massachusetts 02139, United States.; © orcid.org/0000-0002-0575-5045

Jacob A. Erstling – Meinig School of Biomedical Engineering, Cornell University, Ithaca, New York 14853, United States Lara A. Estroff – Department of Materials Science and Engineering and Kavli Institute at Cornell for Nanoscale

Science, Cornell University, Ithaca, New York 14853, United States; orcid.org/0000-0002-7658-1265

Complete contact information is available at: https://pubs.acs.org/10.1021/acs.chemmater.1c01204

Author Contributions

D.V.C. and U.B.W. conceived the overall ideas and study design. D.V.C. conceived of, designed, and experimentally implemented modifications to J.A.H.'s aC' dot synthesis. D.V.C. prepared, imaged, and characterized the neat BCP and nanocomposite films. J.A.H. built the optical microscope used for fluorescence imaging. J.A.E. synthesized and functionalized ATTO488-aC' dots. L.A.E. and U.B.W. helped with data analysis and interpretation. D.V.C. and U.B.W. wrote the manuscript with input of all coauthors.

Funding

This work was funded by the U.S. Department of Energy (DOE), Office of Science, Basic Energy Sciences, under Award No. DE-SC0010560. D.V.C. thanks the National Science Foundation Graduate Research Fellowship Program (NSF GRFP) for providing support under Grant No. DGE-1650441. This work made use of the FEI F20 TEM STEM at the Cornell Center for Materials Research (CCMR) Shared Facilities, which are supported through the NSF MRSEC program under Award No. DMR-1719875.

Notes

The authors declare the following competing financial interest(s): U.B.W. and Cornell University have a financial interest in Elucida Oncology, Inc., which has licensed C dot intellectual property rights generated from the Wiesner labs.

ACKNOWLEDGMENTS

The authors graciously thank all funding sources. D.V.C. thanks CCMR staff member John Grazul for invaluable training and counsel.

REFERENCES

- (1) Pujals, S.; Feiner-Gracia, N.; Delcanale, P.; Voets, I.; Albertazzi, L. Super-Resolution Microscopy as a Powerful Tool to Study Complex Synthetic Materials. *Nat. Rev. Chem.* **2019**, *3*, 68–84.
- (2) Chapman, D. V.; Du, H.; Lee, W. Y.; Wiesner, U. B. Optical Super-Resolution Microscopy in Polymer Science. *Prog. Polym. Sci.* **2020**, *111* (51), 101312.
- (3) Boott, C. E.; Laine, R. F.; Mahou, P.; Finnegan, J. R.; Leitao, E. M.; Webb, S. E. D.; Kaminski, C. F.; Manners, I. In Situ Visualization of Block Copolymer Self-Assembly in Organic Media by Super-Resolution Fluorescence Microscopy. *Chem. Eur. J.* **2015**, *21* (51), 18539–18542.
- (4) Ullal, C. K.; Schmidt, R.; Hell, S. W.; Egner, A. Block Copolymer Nanostructures Mapped by Far-Field Optics. *Nano Lett.* **2009**, 9 (6), 2497–2500.
- (5) Gelissen, A. P. H.; Oppermann, A.; Caumanns, T.; Hebbeker, P.; Turnhoff, S. K.; Tiwari, R.; Eisold, S.; Simon, U.; Lu, Y.; Mayer, J.; Richtering, W.; Walther, A.; Wöll, D. 3D Structures of Responsive Nanocompartmentalized Microgels. *Nano Lett.* **2016**, *16* (11), 7295–7301.
- (6) Friedemann, K.; Turshatov, A.; Landfester, K.; Crespy, D. Characterization via Two-Color STED Microscopy of Nanostructured Materials Synthesized by Colloid Electrospinning. *Langmuir* **2011**, 27 (11), 7132–7139.
- (7) Adelizzi, B.; Aloi, A.; Markvoort, A. J.; Ten Eikelder, H. M. M.; Voets, I. K.; Palmans, A. R. A.; Meijer, E. W. Supramolecular Block Copolymers under Thermodynamic Control. *J. Am. Chem. Soc.* **2018**, 140 (23), 7168–7175.

- (8) Adelizzi, B.; Aloi, A.; Van Zee, N. J.; Palmans, A. R. A.; Meijer, E. W.; Voets, I. K. Painting Supramolecular Polymers in Organic Solvents by Super-Resolution Microscopy. *ACS Nano* **2018**, *12* (5), 4431–4439.
- (9) Zhou, Q. Y.; Fan, C.; Li, C.; Wang, Y. L.; Chen, Z. Q.; Yu, Q.; Zhu, M. Q. AIE-Based Universal Super-Resolution Imaging for Inorganic and Organic Nanostructures. *Mater. Horiz.* **2018**, *5* (3), 474–479.
- (10) Hua, Q. X.; Xin, B.; Xiong, Z. J.; Gong, W. L.; Li, C.; Huang, Z. L.; Zhu, M. Q. Super-Resolution Imaging of Self-Assembly of Amphiphilic Photoswitchable Macrocycles. *Chem. Commun.* **2017**, 53 (18), 2669–2672.
- (11) Li, C.; Yan, H.; Zhao, L. X.; Zhang, G. F.; Hu, Z.; Huang, Z. L.; Zhu, M. Q. A Trident Dithienylethene-Perylenemonoimide Dyad with Super Fluorescence Switching Speed and Ratio. *Nat. Commun.* **2014**, *S* (1), 5709.
- (12) Nevskyi, O.; Sysoiev, D.; Oppermann, A.; Huhn, T.; Wöll, D. Nanoscopic Visualization of Soft Matter Using Fluorescent Diarylethene Photoswitches. *Angew. Chem., Int. Ed.* **2016**, *55* (41), 12698–12702.
- (13) Boott, C. E.; Leitao, E. M.; Hayward, D. W.; Laine, R. F.; Mahou, P.; Guerin, G.; Winnik, M. A.; Richardson, R. M.; Kaminski, C. F.; Whittell, G. R.; Manners, I. Probing the Growth Kinetics for the Formation of Uniform 1D Block Copolymer Nanoparticles by Living Crystallization-Driven Self-Assembly. *ACS Nano* **2018**, *12* (9), 8920–8933
- (14) Gong, W. L.; Yan, J.; Zhao, L. X.; Li, C.; Huang, Z. L.; Tang, B. Z.; Zhu, M. Q. Single-Wavelength-Controlled in Situ Dynamic Super-Resolution Fluorescence Imaging for Block Copolymer Nanostructures via Blue-Light-Switchable FRAP. *Photochem. Photobiol. Sci.* **2016**, *15* (11), 1433–1441.
- (15) Rust, M. J.; Bates, M.; Zhuang, X. Sub-Diffraction-Limit Imaging by Stochastic Optical Reconstruction Microscopy (STORM). *Nat. Methods* **2006**, *3* (10), 793–796.
- (16) Vogelsang, J.; Steinhauer, C.; Forthmann, C.; Stein, I. H.; Person-Skegro, B.; Cordes, T.; Tinnefeld, P. Make Them Blink: Probes for Super-Resolution Microscopy. *ChemPhysChem* **2010**, *11* (12), 2475–2490.
- (17) Ha, T.; Tinnefeld, P. Photophysics of Fluorescent Probes for Single-Molecule Biophysics and Super-Resolution Imaging. *Annu. Rev. Phys. Chem.* **2012**, *63* (1), 595–617.
- (18) Yan, J.; Zhao, L. X.; Li, C.; Hu, Z.; Zhang, G. F.; Chen, Z. Q.; Chen, T.; Huang, Z. L.; Zhu, J.; Zhu, M. Q. Optical Nanoimaging for Block Copolymer Self-Assembly. *J. Am. Chem. Soc.* **2015**, 137 (7), 2436–2439.
- (19) Merdasa, A.; Tian, Y.; Camacho, R.; Dobrovolsky, A.; Debroye, E.; Unger, E. L.; Hofkens, J.; Sundström, V.; Scheblykin, I. G. supertrap" at Work: Extremely Efficient Nonradiative Recombination Channels in MAPbI3 Perovskites Revealed by Luminescence Super-Resolution Imaging and Spectroscopy. ACS Nano 2017, 11 (6), 5391–5404.
- (20) Merdasa, A.; Bag, M.; Tian, Y.; Källman, E.; Dobrovolsky, A.; Scheblykin, I. G. Super-Resolution Luminescence Microspectroscopy Reveals the Mechanism of Photoinduced Degradation in CH3NH3PbI3 Perovskite Nanocrystals. *J. Phys. Chem. C* **2016**, *120* (19), 10711–10719.
- (21) Habuchi, S.; Onda, S.; Vacha, M. Mapping the Emitting Sites within a Single Conjugated Polymer Molecule. *Chem. Commun.* **2009**, No. 32, 4868–4870.
- (22) Duan, J.; Wu, W.; Nolan, A. M.; Wang, T.; Wen, J.; Hu, C.; Mo, Y.; Luo, W.; Huang, Y. Lithium-Graphite Paste: An Interface Compatible Anode for Solid-State Batteries. *Adv. Mater.* **2019**, *31* (10), 1807243.
- (23) Zhang, Q.; Yao, X.; Mwizerwa, J. P.; Huang, N.; Wan, H.; Huang, Z.; Xu, X. FeS Nanosheets as Positive Electrodes for All-Solid-State Lithium Batteries. *Solid State Ionics* **2018**, *318*, *60*–*64*.
- (24) Klähn, S.; Hagemann, M. Compatible Solute Biosynthesis in Cyanobacteria. *Environ. Microbiol.* **2011**, *13* (3), 551–562.

- (25) Seliktar, D. Designing Cell-Compatible Hydrogels for Biomedical Applications. *Science* **2012**, 336 (6085), 1124–1128.
- (26) Faxälv, L.; Ekblad, T.; Liedberg, B.; Lindahl, T. L. Blood Compatibility of Photografted Hydrogel Coatings. *Acta Biomater*. **2010**, *6* (7), 2599–2608.
- (27) Huang, J.; Li, J.; Lyu, Y.; Miao, Q.; Pu, K. Molecular Optical Imaging Probes for Early Diagnosis of Drug-Induced Acute Kidney Injury. *Nat. Mater.* **2019**, *18* (10), 1133–1143.
- (28) Li, J.; Pu, K. Development of Organic Semiconducting Materials for Deep-Tissue Optical Imaging, Phototherapy and Photoactivation. *Chem. Soc. Rev.* **2019**, *48*, 38–71.
- (29) Chen, F.; Ma, K.; Benezra, M.; Zhang, L.; Cheal, S. M.; Phillips, E.; Yoo, B.; Pauliah, M.; Overholtzer, M.; Zanzonico, P.; Sequeira, S.; Gonen, M.; Quinn, T.; Wiesner, U.; Bradbury, M. S. Cancer-Targeting Ultrasmall Silica Nanoparticles for Clinical Translation: Physicochemical Structure and Biological Property Correlations. *Chem. Mater.* 2017, 29 (20), 8766–8779.
- (30) Phillips, E.; Penate-Medina, O.; Zanzonico, P. B.; Carvajal, R. D.; Mohan, P.; Ye, Y.; Humm, J.; Gönen, M.; Kalaigian, H.; Schöder, H.; Strauss, H. W.; Larson, S. M.; Wiesner, U.; Bradbury, M. S. Clinical Translation of an Ultrasmall Inorganic Optical-PET Imaging Nanoparticle Probe. *Sci. Transl. Med.* **2014**, *6* (260), 260ra149.
- (31) Chin, V.; Collins, B. E.; Sailor, M. J.; Bhatia, S. N. Compatibility of Primary Hepatocytes with Oxidized Nanoporous Silicon. *Adv. Mater.* **2001**, *13* (24), 1877–1880.
- (32) Park, C.; Yoon, J.; Thomas, E. L. Enabling Nanotechnology with Self Assembled Block Copolymer Patterns. *Polymer* **2003**, 44 (22), 6725–6760.
- (33) Teraoka, I. *Polymer Solutions: An Introduction to Physical Properties*; John Wiley & Sons, Inc.: New York, NY, U.S.A., 2002; Chapters 1–2, pp 1–166.
- (34) Huang, D.; Liao, F.; Molesa, S.; Redinger, D.; Subramanian, V. Plastic-Compatible Low Resistance Printable Gold Nanoparticle Conductors for Flexible Electronics. *J. Electrochem. Soc.* **2003**, *150* (7), G412–G417.
- (35) Jou, J. H.; Huang, P. T. Compatibility Effect on Moisture Diffusion in Polyimide Blends. *Polymer* **1992**, 33 (6), 1218–1222.
- (36) Stelzig, S. H.; Klapper, M.; Müllen, K. A Simple and Efficient Route to Transparent Nanocomposites. *Adv. Mater.* **2008**, 20 (5), 929–932.
- (37) Hoheisel, T. N.; Hur, K.; Wiesner, U. B. Block Copolymer-Nanoparticle Hybrid Self-Assembly. *Prog. Polym. Sci.* **2015**, *40*, 3–32.
- (38) Goel, V.; Pietrasik, J.; Poling-Skutvik, R.; Jackson, A.; Matyjaszewski, K.; Krishnamoorti, R. Structure of Block Copolymer Grafted Silica Nanoparticles. *Polymer* **2018**, *159*, 138–145.
- (39) Mackay, M. E.; Tuteja, A.; Duxbury, P. M.; Hawker, C. J.; Van Horn, B.; Guan, Z.; Chen, G.; Krishnan, R. S. General Strategies for Nanoparticle Dispersion. *Science* **2006**, 311 (5768), 1740–1743.
- (40) Chiu, J. J.; Kim, B. J.; Kramer, E. J.; Pine, D. J. Control of Nanoparticle Location in Block Copolymers. *J. Am. Chem. Soc.* **2005**, 127 (14), 5036–5037.
- (41) Lin, Y.; Daga, V. K.; Anderson, E. R.; Gido, S. P.; Watkins, J. J. Nanoparticle-Driven Assembly of Block Copolymers: A Simple Route to Ordered Hybrid Materials. *J. Am. Chem. Soc.* **2011**, *133* (17), 6513–6516.
- (42) Listak, J.; Bockstaller, M. R. Stabilization of Grain Boundary Morphologies in Lamellar Block Copolymer/Nanoparticle Blends. *Macromolecules* **2006**, *39* (17), 5820–5825.
- (43) Caruso, F. Nanoengineering of Particle Surfaces. *Adv. Mater.* **2001**, *13* (1), 11–22.
- (44) Kim, B. J.; Bang, J.; Hawker, C. J.; Chiu, J. J.; Pine, D. J.; Jang, S. G.; Yang, S. M.; Kramer, E. J. Creating Surfactant Nanoparticles for Block Copolymer Composites through Surface Chemistry. *Langmuir* **2007**, 23 (25), 12693–12703.
- (45) Kim, B. J.; Fredrickson, G. H.; Hawker, C. J.; Kramer, E. J. Nanoparticle Surfactants as a Route to Bicontinuous Block Copolymer Morphologies. *Langmuir* **2007**, 23 (14), 7804–7809.

- (46) Uzun, O.; Hu, Y.; Verma, A.; Chen, S.; Centrone, A.; Stellacci, F. Water-Soluble Amphiphilic Gold Nanoparticles with Structured Ligand Shells. *Chem. Commun.* **2008**, No. 2, 196–198.
- (47) Provost, A.; Rousset, C.; Bourdon, L.; Mezhoud, S.; Reungoat, E.; Fourneaux, C.; Bresson, T.; Pauly, M.; Béard, N.; Possi-Tchouanlong, L.; Grigorov, B.; Bouvet, P.; Diaz, J. J.; Chamot, C.; Pécheur, E. I.; Ladavière, C.; Charreyre, M. T.; Favier, A.; Place, C.; Monier, K. Innovative Particle Standards and Long-Lived Imaging for 2D and 3D DSTORM. *Sci. Rep.* **2019**, *9* (1), 17967.
- (48) Gao, P.; Liang, Z.; Zhao, Z.; Wang, W.; Yang, C.; Hu, B.; Cui, F. Enhanced Adsorption of Steroid Estrogens by One-Pot Synthesized Phenyl-Modified Mesoporous Silica: Dependence on Phenyl-Organosilane Precursors and PH Condition. *Chemosphere* **2019**, 234, 438–449.
- (49) Yathindranath, V.; Rebbouh, L.; Moore, D. F.; Miller, D. W.; van Lierop, J.; Hegmann, T. A Versatile Method for the Reductive, One-Pot Synthesis of Bare, Hydrophilic and Hydrophobic Magnetite Nanoparticles. *Adv. Funct. Mater.* **2011**, *21* (8), 1457–1464.
- (50) Wang, X.; Xiong, R.; Wei, G. Preparation of Mesoporous Silica Thin Films on Polystyrene Substrate by Electrochemically Induced Sol-Gel Technique. *Surf. Coat. Technol.* **2010**, *204* (14), 2187–2192.
- (51) Ma, K.; Wiesner, U. Modular and Orthogonal Post-PEGylation Surface Modifications by Insertion Enabling Penta-Functional Ultrasmall Organic-Silica Hybrid Nanoparticles. *Chem. Mater.* **2017**, 29 (16), 6840–6855.
- (52) Rong, Y.; Chen, H. Z.; Wu, G.; Wang, M. Preparation and Characterization of Titanium Dioxide Nanoparticle/ Polystyrene Composites via Radical Polymerization. *Mater. Chem. Phys.* **2005**, *91* (2–3), 370–374.
- (53) Ou, B.; Li, D. Preparation of Well-Defined Polystyrene/Silica Hybrid Nanoparticles by ATRP. *Sci. China, Ser. B: Chem.* **2008**, *51* (1), 51–57.
- (54) Khabibullin, A.; Kopeć, M.; Matyjaszewski, K. Modification of Silica Nanoparticles with Miktoarm Polymer Brushes via ATRP. *J. Inorg. Organomet. Polym. Mater.* **2016**, 26 (6), 1292–1300.
- (55) Schmid, A.; Fujii, S.; Armes, S. P. Polystyrene-Silica Nanocomposite Particles via Alcoholic Dispersion Polymerization Using a Cationic Azo Initiator. *Langmuir* **2006**, 22 (11), 4923–4927.
- (56) Nasir, A.; Kausar, A. A Review on Materials Derived from Polystyrene and Different Types of Nanoparticles. *Polym.-Plast. Technol. Eng.* **2015**, 54 (17), 1819–1849.
- (57) Erstling, J. A.; Hinckley, J. A.; Bag, N.; Hersh, J.; Feuer, G. B.; Lee, R.; Malarkey, H. F.; Yu, F.; Ma, K.; Baird, B. A.; Wiesner, U. B. Ultrasmall, Bright, and Photostable Fluorescent Core-Shell Aluminosilicate Nanoparticles for Live-Cell Optical Super-Resolution Microscopy. *Adv. Mater.* 2021, 33 (8), 2006829.
- (58) Ma, K.; Zhang, D.; Cong, Y.; Wiesner, U. Elucidating the Mechanism of Silica Nanoparticle PEGylation Processes Using Fluorescence Correlation Spectroscopies. *Chem. Mater.* **2016**, 28 (5), 1537–1545.
- (59) Kohle, F. F. E.; Hinckley, J. A.; Li, S.; Dhawan, N.; Katt, W. P.; Erstling, J. A.; Werner-Zwanziger, U.; Zwanziger, J.; Cerione, R. A.; Wiesner, U. B. Amorphous Quantum Nanomaterials. *Adv. Mater.* **2019**, *31* (5), 1806993.
- (60) Hinckley, J. A.; Chapman, D. V.; Hedderick, K. R.; Oleske, K. W.; Estroff, L. A.; Wiesner, U. B. Quantitative Comparison of Dye and Ultrasmall Fluorescent Silica Core-Shell Nanoparticle Probes for Optical Super-Resolution Imaging of Model Block Copolymer Thin Film Surfaces. ACS Macro Lett. 2019, 8 (10), 1378–1382.
- (61) Chandrasekhar, V.; Boomishankar, R.; Nagendran, S. Recent Developments in the Synthesis and Structure of Organosilanols. *Chem. Rev.* **2004**, *104* (12), 5847–5910.
- (62) Israelachvili, J.; Pashley, R. The Hydrophobic Interaction Is Long Range, Decaying Exponentially with Distance. *Nature* **1982**, 300 (5890), 341–342.
- (63) Buemi, G. In *Hydrogen Bonding New Insights*; Grabowski, S. J., Ed.; Springer: Dordrecht, Netherlands, 2006; Chapter 2, pp 51–107.
- (64) Ruud, K. A.; Sepeda, J. S.; Tibbals, F. A.; Hrncir, D. C. Synthesis and Structural Characterization of [Ph2Si(OH)OSi(OH)

- Ph2]3·(C4H4N 2)2. The First Crystallographic Evidence for Silanol-Amine Hydrogen Bonding and Its Implications for Organic-Sediment Interactions in Natural Waters. *J. Chem. Soc., Chem. Commun.* **1991**, No. 9, 629–630.
- (65) Kim, B. J.; Bang, J.; Hawker, C. J.; Kramer, E. J. Effect of Areal Chain Density on the Location of Polymer-Modified Gold Nanoparticles in a Block Copolymer Template. *Macromolecules* **2006**, 39 (12), 4108–4114.
- (66) Li, Q.; He, J.; Glogowski, E.; Li, X.; Wang, J.; Emrick, T.; Russell, T. P. Responsive Assemblies: Gold Nanoparticles with Mixed Ligands in Microphase Separated Block Copolymers. *Adv. Mater.* **2008**, *20* (8), 1462–1466.
- (67) Bockstaller, M. R.; Lapetnikov, Y.; Margel, S.; Thomas, E. L. Size-Selective Organization of Enthalpic Compatibilized Nanocrystals in Ternary Block Copolymer/Particle Mixtures. *J. Am. Chem. Soc.* **2003**, *125* (18), 5276–5277.
- (68) Ma, K.; Mendoza, C.; Hanson, M.; Werner-Zwanziger, U.; Zwanziger, J.; Wiesner, U. Control of Ultrasmall Sub-10 Nm Ligand-Functionalized Fluorescent Core-Shell Silica Nanoparticle Growth in Water. *Chem. Mater.* **2015**, 27 (11), 4119–4133.
- (69) Barteau, K. P.; Ma, K.; Kohle, F. F. E.; Gardinier, T. C.; Beaucage, P. A.; Gillilan, R. E.; Wiesner, U. Quantitative Measure of the Size Dispersity in Ultrasmall Fluorescent Organic-Inorganic Hybrid Core-Shell Silica Nanoparticles by Small-Angle X-Ray Scattering. *Chem. Mater.* 2019, 31 (3), 643–657.
- (70) Oleske, K. W.; Barteau, K. P.; Turker, M. Z.; Beaucage, P. A.; Estroff, L. A.; Wiesner, U. Block Copolymer Directed Nanostructured Surfaces as Templates for Confined Surface Reactions. *Macromolecules* **2017**, *50* (2), 542–549.
- (71) Oleske, K. W.; Barteau, K. P.; Beaucage, P. A.; Asenath-Smith, E.; Wiesner, U.; Estroff, L. A. Nanopatterning of Crystalline Transition Metal Oxides by Surface Templated Nucleation on Block Copolymer Mesostructures. *Cryst. Growth Des.* **2017**, *17* (11), 5775–5782.
- (72) Warren, S. C.; DiSalvo, F. J.; Wiesner, U. Nanoparticle-Tuned Assembly and Disassembly of Mesostructured Silica Hybrids. *Nat. Mater.* **2007**, *6* (2), 156–161.
- (73) Bang, J.; Jeong, U.; Ryu, D. Y.; Russell, T. P.; Hawker, C. J. Block Copolymer Nanolithography: Translation of Molecular Level Control to Nanoscale Patterns. *Adv. Mater.* **2009**, *21* (47), 4769–4792.
- (74) Garcia, B. C.; Kamperman, M.; Ulrich, R.; Jain, A.; Gruner, S. M.; Wiesner, U. Morphology Diagram of a Diblock Copolymer Aluminosilicate Nanoparticle System. *Chem. Mater.* **2009**, *21* (22), 5397–5405.
- (75) Zhu, S.; Ma, L.; Wang, S.; Chen, C.; Zhang, W.; Yang, L.; Hang, W.; Nolan, J. P.; Wu, L.; Yan, X. Light-Scattering Detection below the Level of Single Fluorescent Molecules for High-Resolution Characterization of Functional Nanoparticles. *ACS Nano* **2014**, 8 (10), 10998–11006.
- (76) Zhou, L.; Cai, M.; Tong, T.; Wang, H. Progress in the Correlative Atomic Force Microscopy and Optical Microscopy. *Sensors* **2017**, *17* (4), 938.
- (77) Miranda, A.; Gómez-Varela, A. I.; Stylianou, A.; Hirvonen, L. M.; Sánchez, H.; De Beule, P. A. A. How Did Correlative Atomic Force Microscopy and Super-Resolution Microscopy Evolve in the Quest for Unravelling Enigmas in Biology? *Nanoscale* **2021**, *13* (4), 2082–2099.
- (78) Kim, J.; Green, P. F. Directed Assembly of Nanoparticles in Block Copolymer Thin Films: Role of Defects. *Macromolecules* **2010**, 43 (24), 10452–10456.
- (79) Dai, X.; Hou, C.; Xu, Z.; Yang, Y.; Zhu, G.; Chen, P.; Huang, Z.; Yan, L. T. Entropic Effects in Polymer Nanocomposites. *Entropy* **2019**, *21* (2), 186.
- (80) Higgins, J. S.; Lipson, J. E. G.; White, R. P. A Simple Approach to Polymer Mixture Miscibility. *Philos. Trans. R. Soc., A* **2010**, 368 (1914), 1009–1025.
- (81) Shiomi, T.; Yoneda, K.; Imai, K.; Hamada, F.; Nasako, T.; Nakajima, A. Thermodynamics of Polymer Blends of Poly(Vinyl

- Methyl Ether) and Polystyrene. Macromolecules 1990, 23 (1), 229-
- (82) Garcia, D. Fourier-Transform Infrared Study of Polystyrene/Poly(Vinyl Methyl Ether) Blends. *J. Polym. Sci., Polym. Phys. Ed.* **1984**, 22 (1), 107–115.
- (83) Lu, F. J.; Benedetti, E.; Hsu, S. L. Spectroscopic Study of Polystyrene and Polyvinyl Methyl Ether) Blends. *Macromolecules* **1983**, *16* (9), 1525–1529.
- (84) Su, C. S.; Patterson, D. Determination by Gas-Liquid Chromatography of the Polystyrene-Poly (Vinyl Methyl Ether) Interaction. *Macromolecules* **1977**, *10* (3), 708–710.
- (85) Bank, M.; Leffingwell, J.; Thies, C. The Influence of Solvent upon the Compatibility of Polystyrene and Poly (Vinyl Methyl Ether). *Macromolecules* 1971, 4 (1), 43–46.
- (86) Hosny, N. A.; Song, M.; Connelly, J. T.; Ameer-Beg, S.; Knight, M. M.; Wheeler, A. P. Super-Resolution Imaging Strategies for Cell Biologists Using a Spinning Disk Microscope. *PLoS One* **2013**, 8 (10), e74604.
- (87) Chong, F. K.; Coates, C. G.; Denvir, D. J.; McHale, N. G.; Thornbury, K. D.; Hollywood, M. A. Optimization of Spinning Disk Confocal Microscopy: Synchronization with the Ultra-Sensitive EMCCD. In *Three-Dimensional and Multidimensional Microscopy: Image Acquisition and Processing XI*; Conchello, J.-A., Cogswell, C. J., Wilson, T., Eds.; SPIE: 2004; Vol. 5324, pp 65–76.
- (88) Naumov, A. V.; Gorshelev, A. A.; Vainer, Y. G.; Kador, L.; Köhler, J. Far-Field Nanodiagnostics of Solids with Visible Light by Spectrally Selective Imaging. *Angew. Chem., Int. Ed.* **2009**, 48 (51), 9747–9750.
- (89) Naumov, A. V.; Gorshelev, A. A.; Gladush, M. G.; Anikushina, T. A.; Golovanova, A. V.; Köhler, J.; Kador, L. Micro-Refractometry and Local-Field Mapping with Single Molecules. *Nano Lett.* **2018**, *18* (10), 6129–6134.
- (90) Li, G.; Zhu, R.; Yang, Y. Polymer Solar Cells. *Nat. Photonics* **2012**, *6* (3), 153–161.
- (91) Larson, D. R.; Ow, H.; Vishwasrao, H. D.; Heikal, A. A.; Wiesner, U.; Webb, W. W. Silica Nanoparticle Architecture Determines Radiative Properties of Encapsulated Fluorophores. *Chem. Mater.* **2008**, 20 (8), 2677–2684.
- (92) Ovesný, M.; Křížek, P.; Borkovec, J.; Švindrych, Z.; Hagen, G. M. ThunderSTORM: A Comprehensive ImageJ Plug-in for PALM and STORM Data Analysis and Super-Resolution Imaging. *Bioinformatics* **2014**, *30* (16), 2389–2390.
- (93) Kao, T.; Kohle, F.; Ma, K.; Aubert, T.; Andrievsky, A.; Wiesner, U. Fluorescent Silica Nanoparticles with Well-Separated Intensity Distributions from Batch Reactions. *Nano Lett.* **2018**, *18* (2), 1305–1310.
- (94) Demmerle, J.; Wegel, E.; Schermelleh, L.; Dobbie, I. M. Assessing Resolution in Super-Resolution Imaging. *Methods* **2015**, *88*, 3–10.